Comparative study of the Martian suprathermal electron depletions based on Mars Global Surveyor, Mars Express, and Mars Atmosphere and Volatile EvolutioN mission observations

M. Steckiewicz, P. Garnier, N. André, D. L. Mitchell, L. Andersson, E. Penou, A. Beth, A. Fedorov, J. -A. Sauvaud, C. Mazelle, et al.

AGU PUBLICATIONS

JGR

Journal of Geophysical Research: Space Physics

RESEARCH ARTICLE
10.1002/2016JA023205

Special Section:
Major Results From the MAVEN Mission to Mars

Comparative study of the Martian suprathermal electron depletions based on Mars Global Surveyor, Mars Express, and Mars Atmosphere and Volatile EvolutioN mission observations

M. Steckiewicz[1,2], P. Garnier[1,2], N. André[1,2], D. L. Mitchell[3], L. Andersson[4], E. Penou[1,2], A. Beth[5], A. Fedorov[1,2], J.-A. Sauvaud[1,2], C. Mazelle[1,2], D. A. Brain[4], J. R. Espley[6], J. McFadden[3], J. S. Halekas[7], D. E. Larson[3], R. J. Lillis[3], J. G. Luhmann[3], Y. Soobiah[6], and B. M. Jakosky[4]

[1]Université de Toulouse, UPS-OMP, IRAP, Toulouse, France, [2]CNRS, IRAP, Toulouse, France, [3]Space Sciences Laboratory, University of California, Berkeley, California, USA, [4]Laboratory for Atmospheric and Space Physics, University of Colorado Boulder, Boulder, Colorado, USA, [5]Department of Physics, Imperial College London, London, UK, [6]NASA Goddard Space Flight Center, Greenbelt, Maryland, USA, [7]Department of Physics and Astronomy, University of Iowa, Iowa City, Iowa, USA

Key Points:
- Automatic detection of suprathermal electron depletions observed by three spacecraft (MGS, MEX, and MAVEN) during 17 years
- At high altitudes electron depletions are clearly observed by the three spacecraft over crustal magnetic field sources
- At low altitudes interaction with crustal magnetic fields is no longer the dominant creation process for electron depletions

Correspondence to:
M. Steckiewicz,
morgane.steckiewicz@irap.omp.eu

Citation:
Steckiewicz, M., et al. (2017), Comparative study of the Martian suprathermal electron depletions based on Mars Global Surveyor, Mars Express, and Mars Atmosphere and Volatile EvolutioN mission observations, *J. Geophys. Res. Space Physics*, *122*, 857–873, doi:10.1002/2016JA023205.

Received 19 JUL 2016
Accepted 18 NOV 2016
Accepted article online 20 NOV 2016
Published online 9 JAN 2017

Abstract Nightside suprathermal electron depletions have been observed at Mars by three spacecraft to date: Mars Global Surveyor, Mars Express, and the Mars Atmosphere and Volatile EvolutioN (MAVEN) mission. This spatial and temporal diversity of measurements allows us to propose here a comprehensive view of the Martian electron depletions through the first multispacecraft study of the phenomenon. We have analyzed data recorded by the three spacecraft from 1999 to 2015 in order to better understand the distribution of the electron depletions and their creation mechanisms. Three simple criteria adapted to each mission have been implemented to identify more than 134,500 electron depletions observed between 125 and 900 km altitude. The geographical distribution maps of the electron depletions detected by the three spacecraft confirm the strong link existing between electron depletions and crustal magnetic field at altitudes greater than ~170 km. At these altitudes, the distribution of electron depletions is strongly different in the two hemispheres, with a far greater chance to observe an electron depletion in the Southern Hemisphere, where the strongest crustal magnetic sources are located. However, the unique MAVEN observations reveal that below a transition region near 160–170 km altitude the distribution of electron depletions is the same in both hemispheres, with no particular dependence on crustal magnetic fields. This result supports the suggestion made by previous studies that these low-altitudes events are produced through electron absorption by atmospheric CO_2.

1. Introduction

At the present time, Mars does not possess any global dynamo magnetic field. However, localized magnetic fields of crustal origin provide evidence of an ancient dynamo which existed prior to ~4 Ga ago [*Lillis et al.*, 2008, 2013]. These crustal fields can reach intensities exceeding 200 nT at 400 km in the Southern Hemisphere [*Acuña et al.*, 2001]. Hence, Mars does not possess a global intrinsic magnetosphere, but rather several minimagnetospheres induced by closed loops of crustal magnetic field (where magnetic field lines are connected at both ends to the crust). These structures can extend to hundreds of kilometers above the surface with sufficient magnetic pressure to stand off the solar wind flow up to 1000 km [*Brain et al.*, 2003]. The inner magnetic field lines are then isolated from the interplanetary magnetic field (IMF). The magnetic topology near Mars is thus quite complex with closed loops of crustal magnetic field, open field lines connecting the crust to the IMF, and draped field lines unconnected to the crust [*Nagy et al.*, 2003; *Bertucci et al.*, 2003; *Brain et al.*, 2007].

Mars is surrounded by a thin CO_2-dominated atmosphere. The solar extreme ultraviolet radiations impinging the neutral part of this atmosphere lead to the creation of the dayside Martian ionosphere. However, the photoelectrons liberated in the dayside of Mars mainly from ionization of atmospheric CO_2 and O by solar photons are also observed in the nightside hemisphere [*Frahm et al.*, 2006]. The nightside Martian ionosphere is maintained by transport processes from the dayside (e.g., horizontal transport of photoelectrons from dayside to nightside along draped magnetic field lines [*Ulusen and Linscott*, 2008; *Fränz et al.*, 2010]), as well

as by production processes such as electron impact ionization of precipitating magnetosheath electrons [*Fillingim et al*., 2010; *Lillis et al*., 2011; *Lillis and Brain*, 2013].

The nightside ionosphere still remains an unfamiliar and mysterious place. Several studies have shown that the nightside ionosphere is irregular, spotty, faint, and complex [*Zhang et al*., 1990; *Němec et al*., 2010; *Duru et al*., 2011; *Withers et al*., 2012]. Using Mars Global Surveyor (MGS) Electron Reflectometer (ER) measurements, *Mitchell et al*. [2001] first observed that the nightside ionosphere was punctuated by abrupt drops of the instrumental count rate by up to 3 orders of magnitude to near-background levels across all energies, hence calling them "plasma voids." These structures seemed to be observed where closed crustal magnetic loops existed at 400 km on the nightside; i.e., they did not connect with the magnetotail, and hence, tail electrons could not access them. On the dayside, these loops can trap ionospheric plasma, including suprathermal photoelectrons. When they travel to the nightside, the electrons are removed through a combination of outward diffusion, scattering, and interactions with the collisional thick atmosphere at lower altitudes. Meanwhile, the external sources of plasma (solar wind plasma traveling up the magnetotail and ionospheric plasma) are excluded from the inner layers of the closed field regions, so that sinks overpass sources, thus creating plasma voids. The topology of the crustal magnetic fields can therefore significantly influence the structure of the nightside ionosphere.

Based on 144 passages of the Mars Express (MEX) spacecraft at low altitudes, *Soobiah et al*. [2006] observed thanks to the Analyser of Space Plasmas and Energetic Atoms that the electron flux underwent significant changes close to crustal magnetic fields. Intensified flux signatures were observed mainly on the dayside, whereas flux depletions were features of the nightside hemisphere. Through a study over 7.5 years of the MGS mission, *Brain et al*. [2007] showed statistically that plasma voids are indeed concentrated near strong crustal magnetic fields and that very few voids are seen at large distances from crustal magnetic sources. This study also revealed that plasma voids are surrounded by areas with trapped and conic electron pitch angle (angle between the electron velocity and the magnetic field vectors) distributions, consistent with the idea of closed magnetic field lines and indicating that the outer layers of closed magnetic field regions are populated thanks to source processes such as reconnection with the draped IMF.

Furthermore, the long-term statistical survey by *Brain et al*. [2007] highlighted that hardly any plasma voids are observed on the dayside (defined as solar zenith angle (SZA) greater than 90°). This means that when the crustal magnetic loops rotate to the dayside, they trap newly created ionospheric plasma. As the ionospheric plasma is homogeneously created in the dayside, voids are essentially never seen on this side of Mars. While plasma voids are restricted to the nightside, studies made with MEX data by *Soobiah et al*. [2006] and *Duru et al*. [2011] showed no dissymmetry between the dawnside and the duskside. Plasma voids are globally distributed regardless of nightside local time (1800 h–2400 h and 0000 h–0600 h), within the limits of their studies.

Crustal magnetic loops do not necessarily stay closed as the planet rotates [*Ma et al*., 2014], and crustal fields can connect and reconnect with the piled-up, draped, and dynamic IMF. Hence, when they travel to the nightside, regions with strong enough horizontal crustal fields are able to stand off the IMF effects. The crustal magnetic loops in these regions thus stay closed all the way across the nightside and are populated by permanent plasma voids, which means that we can observe this phenomena during each passage above such regions on the nightside. On the other hand, regions with weaker horizontal fields are essentially intermittently populated with plasma voids, depending on the external drivers. For low and moderate solar wind pressure crustal magnetic loops are closed and devoid of plasma. However, for high solar wind pressure the crustal field lines open up and get connected to the IMF. These weak crustal magnetic field regions are then filled with solar wind plasma travelling through the tail [*Lillis and Brain*, 2013].

More recently, *Hall et al*. [2016] used the rapid reductions of a proxy measurement of the electron flux derived from the MEX ASPERA-3 Electron Spectrometer (ELS) electron flux measurements integrated across the 20–200 eV energy range to automatically identify plasma voids. The study covers approximately 10 years of the MEX mission from 2004 to 2014 and is restricted to the illuminated induced magnetosphere (region of space inside the magnetic pileup boundary and outside the cylindrical shadow of the planet). Using this method, plasma voids were detected among 56% of the orbits under study, from 266 km (MEX lowest periapsis) to 10 117 km. A statistical study of the distribution of these events showed that approximately 80% of them occurred below 1300 km, predominantly at SZA between 90° and 120°. Study of the spatial

and altitudinal distributions of the detected plasma voids confirmed the strong link existing between the plasma void occurrence and the magnitude of the crustal magnetic field. The bigger the source was, the higher plasma voids could be observed. However, some regions appear to be in contradiction with this global behavior, which suggests that other processes are involved in plasma void creation such as the interaction between the solar wind and the Martian plasma.

All these results have been obtained from MGS and MEX data that have several constraints. MGS did not carry any ion spectrometer and was fixed in local time at 02:00 A.M./02:00 P.M. via a circular orbit (altitude between 370 and 430 km). MEX on the other hand does not carry any magnetometer and has a periapsis between 245 and 365 km. The Mars Atmosphere and Volatile EvolutioN (MAVEN) spacecraft entered into orbit around Mars in September 2014 with a complete suite of plasma and field instruments, including a magnetometer, two ion and one electron spectrometers. The altitude of the spacecraft reaches 150 km during nominal orbits and is periodically lowered down to 125 km for 5 days periods known as "deep dips" [*Bougher et al*., 2015], which allows measurements of these plasma phenomena at previously unsampled altitudes. Initial results on the plasma voids observed by MAVEN above the Northern Hemisphere was then investigated by *Steckiewicz et al*. [2015]. At the time of that initial study, the data available were restricted to latitudes between 20°N and 74°N. This multiinstrument study leads to rename the "electron plasma voids" into "nightside suprathermal electron depletions" (hereinafter referred as electron depletions). It suggested that the distribution of electron depletions is highly dependent on altitude. Above a transition region near 160–170 km altitude, electron depletions are strongly linked to horizontal crustal magnetic fields as previously shown by MEX and MGS observations. However, below that transition region the distribution was found to be more homogeneous, irrespective of crustal magnetic field sources. Thus, two main electron sinks leading to the creation of electron depletions have been identified: the exclusion by closed crustal magnetic loops and the absorption by atmospheric CO_2. These two processes seem to always play a role in electron depletions creation but have two different predominance areas: the exclusion by closed crustal magnetic sources is predominant at high altitudes, whereas absorption by atmospheric CO_2 is predominant at low altitudes.

The present paper takes advantage of the different characteristics of these three missions to study the geographical and altitudinal distributions of electron depletions from different points of view. MGS data are used from 1999 to 2006 in order to take advantage of the mapping circular orbit at a roughly constant altitude (~400 km) of the spacecraft, allowing observations of the phenomenon every 2 h over the whole range of possible latitudes [−90°, 90°]. MEX data are used from 2004 to 2014, which gives us an unparalleled long-term view of the phenomenon at both relatively low (down to ~300 km) and high altitudes. Finally, MAVEN data are used from October 2014 to November 2015. During this time period the spacecraft covered both hemispheres except the poles, but due to this short duration and MAVEN orbital parameters, all latitudes are not yet covered at all possible altitudes. Even though the coverage and duration of this data set are much lower than those of MGS and MEX, MAVEN reached during this time period altitudes down to 125 km, which are unsampled by MGS nor MEX.

This huge data set gathering observations made over 17 years by different instruments reaching different altitude regimes enables us to compare events observed in similar conditions (several spacecraft in the same region) and enrich this joint vision with new observations closer to the surface (with MAVEN). We first show examples of how electron depletions are observed by MGS, MEX, and MAVEN, then describe the three criteria used to automatically detect electron depletions in each mission electron spectrometer measurements. An exhaustive data set of electron depletions derived from these three criteria is then used to compare their geographical distribution with the location of crustal magnetic sources. We finally investigate and compare the altitude distributions obtained with MAVEN and MEX, before a conclusion ends the paper.

2. Three Spacecraft, Three Different Perspectives of Suprathermal Electron Depletions

Martian suprathermal electron depletions have been observed to date by three spacecraft: MGS, MEX, and MAVEN. The last two are still in good operating condition at the time of writing. Figures 1–3 display the plasma observations of these structures made chronologically by MGS, MEX, and MAVEN, respectively, and are described next in more details. The improved performances of the plasma instrument suite over the different missions allow now for a more accurate understanding of electron depletions.

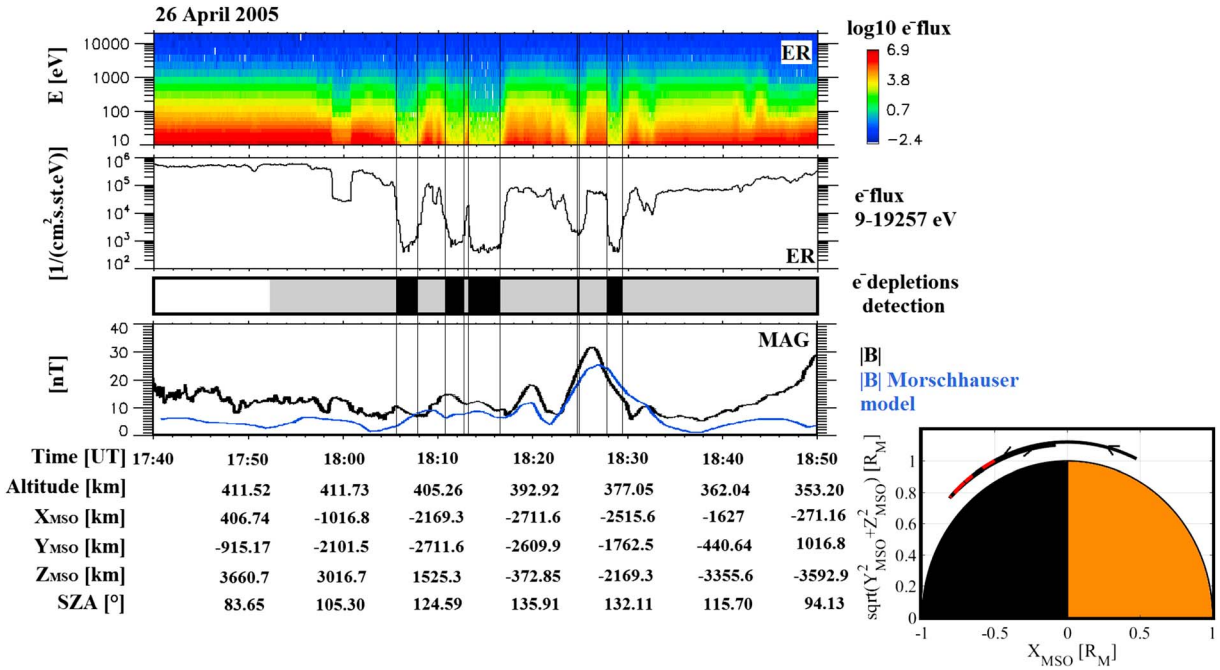

Figure 1. Example of electron depletion observed by MGS on 26 April 2005. (first panel) ER energy-time spectrogram of omnidirectional electron flux. (second panel) ER omnidirectional electron flux summed over all energies available (11–16127 eV). (third panel) Detection of electron depletions by criterion (3) (black boxes). See section 3 for more details. The shadow corresponds to the nightside. (fourth panel) Magnetic field intensity (measured by MAG in black and calculated from the model of Morschhauser in blue). (fifth panel, bottom right) MGS orbital trajectory in a cylindrically symmetric MSO coordinate frame. The locations of the electron depletions detected are highlighted in red. The altitude is defined with respect to a sphere with the Mars' volumetric mean radius of 3389.51 km.

All the ephemerides used in this paper are expressed in the Mars-centric Solar Orbital (MSO) coordinates defined as follows: the origin is the center of Mars, the x axis points from the center of Mars to the Sun, y points opposite to Mars' orbital angular velocity, and z completes the right-handed set so that the frame rotates slowly as Mars orbits the Sun. The nightside is here considered as $x < 0$. However, the real border between sunlit and dark sides occurs at different SZA for different altitudes. Hence, if an electron depletion is observed in the nightside, it can be to some extent in the illuminated terminator region.

2.1. MGS: First Observations

The Mars Global Surveyor spacecraft was placed in its mapping orbit around Mars on 9 March 1999 [*Albee et al.*, 2001]. This orbit was nearly circular, Sun-synchronous, near-polar, and at an altitude varying between 368 and 438 km, which corresponded to a period of approximately 2 h. The orbit was also fixed at a local time of 02:00 A.M./02:00 P.M. Contact with the spacecraft was lost in early November 2006. The MGS magnetic field experiment was composed of two redundant triaxial fluxgate magnetometers (MAG) and an Electron Reflectometer (ER) [*Acuña et al.*, 2001]. MAG was able to detect ambient magnetic fields from ± 4 nT to $\pm$ 65 ,536 nT, and ER measured electrons in 19 logarithmically spaced energy channels ranging from 10 eV to 20 keV with an energy resolution of $\frac{\delta E}{E} = 25\%$ (full width at half maximum). MGS did not carry an ion spectrometer.

Figure 1 shows an example of electron depletions observed by MGS on 26 April 2005. The first panel is the ER energy-time spectrogram of omnidirectional electron flux, and the second panel is the ER electron flux summed over all the observed energies. The blacked out regions in the third panel delineate the electron depletions automatically detected by criterion (3), when the electron flux drops by more than 2 orders of magnitude at all observed energies. This criterion is described in more details in section 3.3. The fourth panel is the magnitude of the magnetic field measured by MAG (black profile) superimposed with the magnitude of the crustal magnetic field calculated from the model of *Morschhauser et al.* [2014] (blue profile; hereinafter referred as the Morschhauser model). Thus, the first three depletions (between 18:05 and 18:15) are located over weak crustal field regions, whereas the two last (between 18:25 and 18:30) are located over a modest

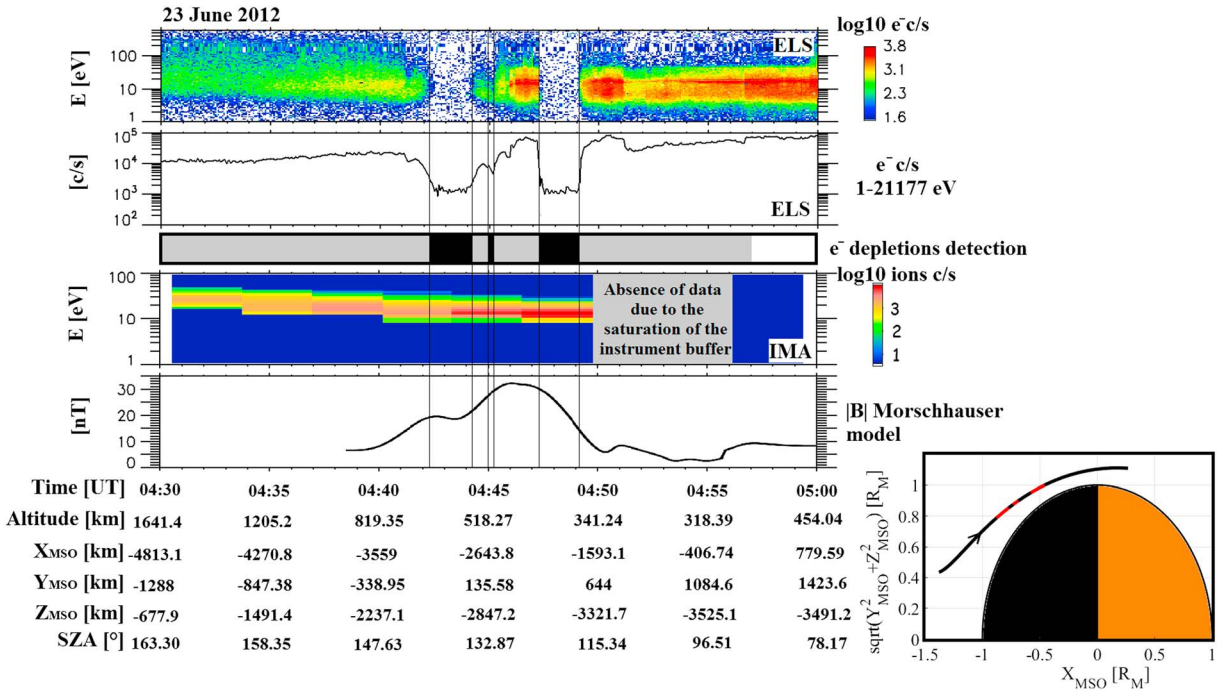

Figure 2. Example of electron depletion observed by MEX on 23 June 2012. (first panel) ELS energy-time spectrogram of omnidirectional electron counts per second. (second panel) ELS electron counts per second summed over all the energies available (1–21177 eV). (third panel) Detection of electron depletions by criterion (2) (black boxes). See section 3 for more details. The shadow corresponds to the nightside. (fourth panel) IMA energy-time spectrogram of omnidirectional heavy ions counts per second (m/q > 20). (fifth panel) Magnetic field intensity calculated from the Morschhauser model. (sixth panel, bottom right) MEX orbital trajectory in a cylindrically symmetric MSO coordinate frame. The locations of the electron depletions detected are highlighted in red.

crustal magnetic field source (~25 nT at 400 km altitude). On the last bottom right plot, the orbital trajectory of MGS in a cylindrically symmetric MSO coordinate frame is plotted. The depletions are highlighted in red and are all located on the nightside.

As shown in this example, the electron flux measured by ER inside the electron depletions is barely above the background level (see Figure 10 of *Mitchell et al.* [2001] for a detailed description of the background level) at all energies observed, which lead *Mitchell et al.* [2001] to designate them as plasma voids.

2.2. Mars Express

The Mars Express spacecraft was inserted into orbit around Mars in January 2004. Its orbit is highly elliptical, with a periapsis altitude between 245 and 365 km and an apoapsis altitude of ~10,000 km, which implies a period of ~6.75 h. The inclination of the orbit is 86°, and it precesses slowly [*Chicarro et al.*, 2004]. The ASPERA-3 experiment is composed of four instruments including the Electron Spectrometer (ELS) and the Ion Mass Analyzer (IMA) [*Barabash et al.*, 2004]. The IMA sensor measures 3-D fluxes of different ion species with a mass-to-charge ratio (m/q) resolution of 1, 2, 4, 8, 16, and >20 in the energy range of 0.01–30 keV/q, with an energy resolution of $\frac{\delta E}{E} = 7\%$. The ELS instrument measures the electron fluxes in the energy range of 0.001–20 keV/q in 128 logarithmically spaced energy channels with an energy resolution of $\frac{\delta E}{E} = 8\%$ (which is the best energy resolution among the electron spectrometers of the three spacecraft; see Table 1). In general, ELS has been operated in four different modes (default/survey mode, linear mode, 1 s mode, and 32 Hz mode), differing mainly in the energy ranges, the energy steps, and the measuring cadences used (see *Frahm et al.* [2006] and *Hall et al.* [2016] for more details about the different ELS modes). In this study, we only include measurements when ELS is operating in survey mode. Mars Express does not carry a magnetometer.

Figure 2 shows an example of electron depletions observed by MEX on 23 June 2012. The first panel is the ELS energy-time spectrogram of omnidirectional electron counts per second, and the second panel is the ELS

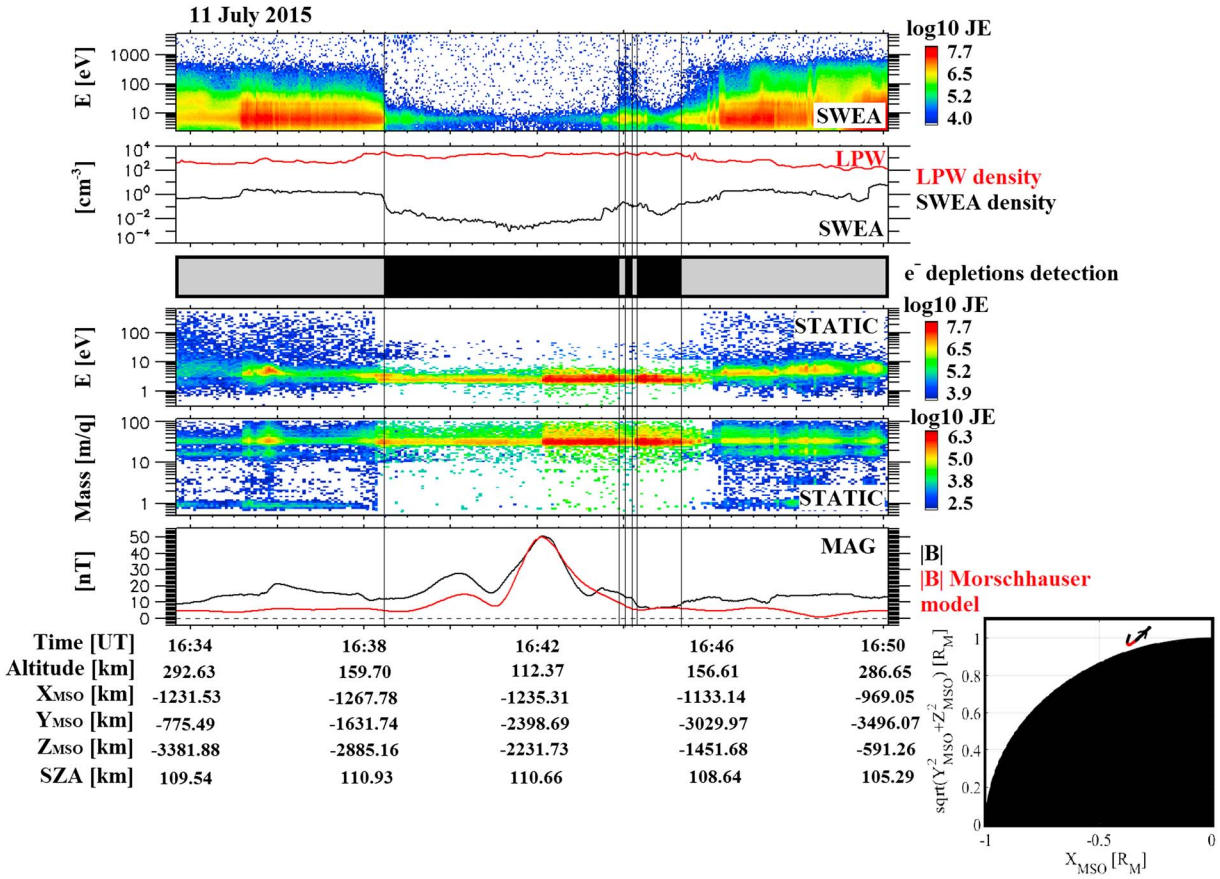

Figure 3. Example of electron depletion observed with MAVEN. (first panel) SWEA energy-time spectrogram of omnidirectional electron energy flux (ENGY mode) corrected for the potential measured with LPW. (second panel) Electron density calculated with SWEA (black) superimposed with the density calculated with LPW (red). (third panel) Detection of electron depletions by criterion (1) (black boxes). See section 3 for more details. The shadow corresponds to the nightside. (fourth panel) STATIC energy-time spectrogram of omnidirectional ion energy flux (C0 mode). (fifth panel) STATIC mass-time spectrogram of omnidirectional ion energy flux (C6 mode). (sixth panel) Magnetic field intensity (measured by MAG in black and calculated from the model of Morschhauser in red). (seventh panel, bottom right) MAVEN orbital trajectory in a cylindrically symmetric MSO coordinate frame. The locations of the electron depletions detected have been highlighted in red.

omnidirectional electron counts per second summed over all the available energies. Note that ELS's geometric factor is approximately fixed, so that counts are proportional to electron flux. The blacked out regions in the third panel delineate the electron depletions automatically detected by criterion (2), when the electron count drops abruptly by more than 2 orders of magnitude at all the considered energies and thus reaches the background noise level (~40 c/s). This criterion is described in more details in section 3.2. The fourth panel is the energy-time spectrogram of the omnidirectional heavy ions counts per second (m/q >20) measured by IMA. There are few light ions detected (not shown), but we can see that electron depletions are filled with heavy ions (mainly O_2^+ and CO_2^+ at this altitude in the nightside [*Krasnopolsky*, 2002]), having an energy E/q of a dozen of eV. Hence, we cannot name these structures plasma voids anymore but still "electron plasma voids." As there is no magnetometer on board MEX we plot on the fifth panel the magnitude of the crustal magnetic field calculated from the model of Morschhauser as a guide. As for the MGS case, the three electron depletions are located above a medium crustal magnetic area (35 nT at 500 km altitude). On the last bottom right plot, the orbital trajectory of MEX in a cylindrically symmetric MSO coordinate frame is plotted. The depletions are highlighted in red and are all located on the nightside.

2.3. MAVEN

The MAVEN spacecraft entered into orbit around Mars on 21 September 2014 [*Jakosky et al.*, 2015]. Its orbit is elliptical with an inclination of 74°, a periapsis altitude of 150 km (with four strategically located "deep-dip" campaigns during which the periapsis was lowered to 125 km), and an apoapsis altitude of 6200 km, which

Table 1. Summary of the Characteristics of the Magnetometer, Electron Spectrometer, Ion Spectrometer, and Langmuir Probe On Board MGS, MEX, and MAVEN

Instrument Type	Quantity	MGS	MEX	MAVEN
Magnetometer	Magnitude range	4–65,536 nT	None	0.06–65,536 nT
Electron spectrometer	Energy range	10–20,000 eV	1–20,000 eV	3–4,600 eV
	Energy resolution	25%	8%	17%
Ion spectrometer	Energy range	None	10–30,000 eV/q	0.1–30,000 eV/q
	Energy resolution		7%	16%
	Mass range		1, 2, 4, 8, 16, and >20 m/q	H^+, He^{++}, He^+, O^+, O_2^+, and CO_2^+
Langmuir probe	Temperature	None	None	0.05 to 5 eV

implies a period of 4.5 h. During the first year of the primary mission, the orbit precessed so that the periapsis and apoapsis points visited a wide range of longitudes, latitudes, SZAs, and local times.

The MAVEN particles and fields package is composed of seven instruments, including the Suprathermal and Thermal Ion Composition (STATIC) analyzer, the Solar Wind Electron Analyzer (SWEA), the Langmuir Probe and Waves (LPW), and the Magnetometer (MAG). STATIC operates over an energy range of 0.1 eV to 30 keV with an energy resolution of $\frac{\delta E}{E} = 16\%$ and a nominal time resolution of 4 s [*McFadden et al.*, 2015]. It is able to resolve H^+, He^{++}, He^+, O^+, O_2^+, and CO_2^+ ions. SWEA can measure the energy and angular distributions of 3–4600 eV electrons with an energy resolution of $\frac{\delta E}{E} = 17\%$ [*Mitchell et al.*, 2016]. LPW is designed to measure the temperature and density of thermal ionospheric electrons, which have temperatures (*Te*) ranging from 0.05 to 5 eV [*Andersson et al.*, 2015], as well as the spacecraft potential. MAG consists of two identical triaxial fluxgate sensors, which can measure the magnitude and direction of the ambient magnetic field from 0.06 to 65,536 nT [*Connerney et al.*, 2015]. All these characteristics are recorded in Table 1 so that they can be compared with those of MGS and MEX instruments.

Figure 3 shows an example of an electron depletion observed with MAVEN on 11 July 2015. The first panel is the SWEA energy-time spectrogram of omnidirectional electron energy flux (also referred to as JE in Figure 3). Similarly to the examples shown for MEX and MGS, the blacked out regions in the third panel delineate the electron depletions automatically detected by criterion (1), when the electron flux at all the considered energies drop abruptly by more than 2 orders of magnitude. This criterion is described in more details in section 3.1. However, we can see that there is a remaining electron population at approximately 6–7 eV, which could not be observed by MGS due to its energy range and by MEX probably due to higher negative spacecraft potential. Moreover, the third panel shows the density calculated from SWEA data in black and the density from LPW in red. Note that during this time interval the quality flag of the LPW density and of the spacecraft potential used for the calculation of the density from SWEA data is always greater than 50 except for 16:37:55 (in the ionosphere) and 16:45:20 (at the end of the depletion), which means that these data are reliable (L. Andersson, private communication). Due to instrumental limits the density calculated with SWEA data is restricted to electrons with energies greater than 3 eV (see Table 1), whereas the density calculated with LPW includes lower-energy electrons, which explains the difference observed between the two densities (in particular in the ionosphere where the plasma is essentially cold). The characteristic drop in the suprathermal electron flux is very clear in the SWEA density during the electron depletion, whereas there is no drop in LPW density, i.e., in thermal electron density, which even increases slightly.

On the fourth and fifth panels, the STATIC energy-time spectrogram of omnidirectional ion energy flux and the STATIC mass-time spectrogram of omnidirectional ion energy flux are plotted. Thus, the electron depletion is mainly filled with O_2^+ (32 m/q) at 3 eV. This is consistent with the expected ionosphere composition at this altitude and with the energy corresponding to the ram velocity given by the spacecraft to cold O_2^+. Hence, the depletions are not entirely void of plasma, as suggested in the MEX example. Only suprathermal electrons with energies greater than 10 eV are depleted, which justifies the name "suprathermal electron depletions" given by *Steckiewicz et al.* [2015].

The sixth panel shows the magnetic field intensity measured by MAG (black profile) superimposed with the intensity of the crustal magnetic field calculated from the model of Morschhauser (red profile). In this example, the depletions are observed above a moderate crustal magnetic source (50 nT at 125 km). As for MGS and

MEX, on the last bottom right plot, the orbital trajectory of MEX in a cylindrically symmetric MSO coordinate frame is plotted. The depletions are highlighted in red and are all located on the nightside.

3. Criteria Used to Automatically Detect Electron Depletions

Electron depletions can be observed by MGS, MEX, and MAVEN, respectively, on ER, ELS, and SWEA spectrograms. We present here the three criteria, adapted to each set of data, used to automatically detect electron depletions. The starting point of the definition of these criteria is the criterion developed in *Steckiewicz et al*. [2015] for the MAVEN/SWEA data. We thus first explain how this criterion is used for MAVEN before adapting it to MEX and MGS and their own specificities. The application of these three criteria leads to three catalogs of electron depletions used in the next sections to compare the electron depletion distributions as observed by the three spacecraft.

3.1. MAVEN

For MAVEN SWEA data we use the same criterion as in *Steckiewicz et al*. [2015] and given in equation (1). It is based on electron count rates (CR) from SWEA observations and relies on three energy channels ($E_1 = 4.26$ eV, $E_2 = 98.93$ eV, and $E_3 = 111.16$ eV). The numerator gives the count rate at an energy of E_i (per time step), whereas the denominator gives the mean count rate at the same energy over a 1 h period centered on the current time step. This simple criterion thus gives an idea of how the electron flux is at the current time step compared to average conditions. An electron depletion is detected if a ratio of 2 orders of magnitude is identified. These three channels have been chosen after looking at the electron spectrum inside the electron depletions. As seen in Figure 3, inside the electron depletions there is a remaining electron population peaked at 6 eV and hardly any electrons above 10 eV. Hence, we chose an energy channel below 6 eV, and two above to give more weight to depletions of high-energy electrons and to avoid a significant influence by the 6 eV electrons due to spacecraft charging. Usually, the spacecraft potential in the nightside ionosphere is approximately −2 V. This implies a little modification in the energies detected, which are reduced by the same amount. These small potentials have no significant impact on the criterion results. However, some strong spacecraft-charging events can bring the spacecraft potential to a dozen of volts. The electron flux detected at 6 eV during these events is then much lower than the mean electron flux calculated over 1 h, and an electron depletion can be detected. A few cases have been found during the time period under study and have been removed by hand. The sampling time step used for the criterion is the same as the measurement cadence of the SWEA instrument: 4 s. Consequently, the electron depletions detected last at least 4 s, which corresponds to a maximum of 16 km traveled by the spacecraft when at the periapsis.

$$\frac{1}{3}\sum_{i=1}^{3}\frac{\mathrm{CR}(E_i)}{<\mathrm{CR}(E_i), 1h>} < 0.01 \tag{1}$$

The criterion specified in equation (1) worked well for electron depletions in the Northern Hemisphere as shown in *Steckiewicz et al*. [2015]; it is thus also used here in the Southern Hemisphere. The example proposed in Figure 3 illustrates how the criterion detects the electron depletions in agreement with the SWEA spectrogram. Criterion (1) has been applied from 7 October 2014 to 25 November 2015 with no restriction on the nightside nor on the altitude, which corresponds to more than 2000 orbits.

During this time interval electron depletions have only been detected during two specific periods when the spacecraft reaches low altitudes (<900 km) in the nightside. Although MAVEN reached higher altitudes in the induced magnetosphere, criterion (1) detected no depletion above 900 km nor on the dayside. These two periods can be described in terms of aerographic coverage as the following:

1. from October 2014 to April 2015 during which the periapsis was above the Northern Hemisphere;
2. from May 2015 to November 2015 during which the periapsis was above the Southern Hemisphere.

Both of these time periods did not cover the equatorial region and not all local times due to orbital limitations. Over the next few years of the MAVEN mission, the spacecraft will have covered the entire surface of Mars, all local times, and solar zenith angles. The application of this criterion to the time interval under study

resulted in a data set of 1742 electron depletions identified above the Northern Hemisphere and 1956 ones identified above the Southern Hemisphere. We thus detected a lot of electron depletions per orbit. A median value of four depletions observed per orbit has been found. In terms of altitude distribution, the electron depletions detected are observed from 110 km up to 900 km altitude above the strongest crustal magnetic sources. The altitude distribution will be investigated in more details in section 5.

3.2. Mars Express

Based on our experience with MAVEN data, we adapted criterion (1) to MEX ELS data to obtain criterion (2). In this case we use the three following energy channels: $E_1 = 21.20$ eV (for low energies), $E_2 = 95.04$ eV, and $E_3 = 103.25$ eV (for high energies). Thus, by taking a minimum energy above 20 eV, we prevent most of the spacecraft-charging effects to impact results of criterion (2) (see *Fränz et al*. [2006] and *Hall et al*. [2016] for more details concerning spacecraft-charging impacts on ELS spectrograms). We also modify the threshold ratio from 1% to 2% based on the observations of ELS data. The time period under study for MEX data is from 1 March 2004 to 31 December 2014, which is similar to the one studied by *Hall et al*. [2016]. This corresponds to approximately 14,072 orbits. However, we only applied criterion (2) on time intervals longer than 1 h when ELS was working in the survey mode, which corresponds to 9983 time intervals. The time period under study is long enough to allow the periapsis to cover the whole surface of Mars between latitudes of −86° and +86° and all the local times in the nightside thanks to the precessing orbit of MEX. The sampling time step used for the criterion is the same as the measurement cadence of the ELS instrument when operated in its default survey mode: 4 s. Consequently, the electron depletions detected last at least 4 s, which corresponds to a maximum of 17 km in the spacecraft orbital direction when at periapsis.

$$\frac{1}{3}\sum_{i=1}^{3}\frac{\mathrm{CR}(E_i)}{<\mathrm{CR}(E_i), 1h>} < 0.02 \tag{2}$$

The application of this criterion with no restriction on the altitude nor on the nightside resulted in a time table of 17,592 electron depletions. The example proposed in Figure 2 illustrates how the criterion detects the electron depletions in agreement with the ELS spectrogram. Those depletions are detected from 245 km to ~10,000 km both on the nightside and on the dayside (for a small amount of cases). Globally, the depletions have been detected as in the MAVEN case during specific time periods when the periapsis went across the nightside at low enough altitudes. However, most of the depletions observed on the dayside and at altitudes above 1000 km have to be considered with caution (since they include very short data gaps and the lobes—the region located on either side of the plasma sheet with reduced particle fluxes—that cannot be easily excluded). We therefore chose to only consider for the next studies depletions observed in the nightside below 900 km, which is consistent with our MAVEN results and enables the two studies to be compared. With these restrictions, 14,517 depletions have been found on 2197 orbits, which implies a strong presence of spikes in MEX data as in the example in Figure 2. A median value of five depletions observed per orbit has been found.

3.3. Mars Global Surveyor

For the study of the electron depletions observed with MGS we only focus on the data obtained during the circular mapping orbit phase at an altitude of ~400 km. The data set covers the time period from 10 March 1999 to 11 October 2006, which represents more than 42,000 orbits. Such statistics average all the effects of external drivers on electron depletions so that we only see the general behavior of the electron depletions. As the MGS orbit was circular at 400 km, electron depletions can potentially be observed during each orbit. This data set covers the entire surface of Mars but only the 02:00 A.M. local time sector. ER data have a time resolution of 2 s, which corresponds to ~7 km traveled by the spacecraft.

In the case of MGS, a criterion based on three energy channels (one low and two high) does not work well, probably due to the energy resolution of 25%. Hence, we decided to compare the measured omnidirectional flux summed over all the available energies [11 eV; 16,127 eV] every 2 s with the same product averaged over two orbits (4 h). An electron depletion is detected if this ratio is less than 1%, which corresponds to a drop of 2

Table 2. Characteristics of the Electron Depletion Catalogs Derived From the Electron Spectrometer Data of MGS, MEX, and MAVEN

	MGS	MEX	MAVEN
Number of orbits under study[a]	42,048	9,983	2,138
Number of depletions detected[b]	116,278	14,517	3,698
Number of orbits containing depletions	29,460	2,197	899
Median number of depletions per orbit	4	5	4

[a]For MEX it corresponds to the number of time intervals longer than 1 h when ELS was in the survey mode. It corresponds approximately to the number or orbits studied.
[b]The number of depletions detected by criterion (3) for MGS, criterion (2) for MEX and criterion (1) for MAVEN.

orders of magnitude in the electron flux. The MGS criterion is described in equation (3) with a similar form to equations (1) and (2). Consequently, the electron depletion detected size is at least 7 km in the orbital direction.

Among the energy range [11 eV; 16,127 eV], the three channels which collected the majority of the flux were 90–148 eV, 148–245 eV, and 245–400 eV. Electron depletions thus show up in those three most reliable energy channels which are far too high energy to be affected by any spacecraft charging, which would almost always be less than ~20 eV. Hence, the way criterion (3) has been defined makes it insensitive to spacecraft charging.

$$\frac{\mathrm{Flux}(\,[11\ \mathrm{eV}; 16,127\ \mathrm{eV}]\,)}{<(\mathrm{Flux}(\,[11\ \mathrm{eV}; 16,127\ \mathrm{eV}])\,,\ 4\ \ \mathrm{h})>} < 0.01 \tag{3}$$

The example proposed in Figure 1 illustrates how the criterion detects the electron depletions in agreement with the ER spectrogram. However, we can notice that all the decreases that can be observed in the second panel are not detected as electron depletions. This is due to the threshold of 1% chosen. The application of this criterion resulted in a time table of 116,278 electron depletions, which means that, as for MAVEN and MEX, several electron depletions can be detected during a single orbit as in the example shown in Figure 1. Almost all these electron depletions have been detected in the nightside, except few (less than 100) isolated cases. A median value of four depletions observed per orbit has been obtained, as it was found for MAVEN events (Table 2). The median number of depletions per orbit for MEX data is a slightly higher but remains similar to both MAVEN and MGS, which confirms that the occurrence of the electron depletions is stable during the three periods and consistent among the three spacecraft.

4. Geographical Distribution Maps of Electron Depletions

It was observed with MEX and MGS that the electron depletions mainly coincide with strong horizontal crustal fields. With MAVEN data *Steckiewicz et al.* [2015] showed that in the Northern Hemisphere the electron depletions are strongly linked with crustal magnetic field only above a transition region near 160–170 km altitude, whereas below this altitude, they are more homogeneously scattered irrespective of crustal source locations. Thanks to the three catalogs obtained after application of the three criteria described above, we created geographical distribution maps of electron depletions detected by MGS and MEX above all the Martian surface and by MAVEN, which now covers the Northern and Southern Hemispheres except the poles and the equatorial region. In the next three subsections we present the geographical distributions obtained with the three spacecraft whose periapsis decreased from MGS to MAVEN. We start with a mean altitude of 400 km with MGS, then go down to 300 km with MEX, and finally reach altitudes of 125 km with MAVEN.

4.1. MGS

Figure 4 shows the density map of the geographical location of the electron depletions detected with criterion (3). The latitude-longitude map of Mars is detailed in spatial bins of 1° by 1°. For each bin we scored the number of time steps when electron depletions are detected and divided it by the total number of time steps per bin with MGS on the nightside. There are on average more than 1000 time steps when MGS is in the nightside per bin. The color code corresponds to the percentage of electron depletions detected per MGS passage on the nightside. We have also superimposed logarithmically spaced (between 10 and 100 nT) contour lines of the horizontal crustal field calculated at 400 km altitude from the Morschhauser model.

We can see that, globally, the electron depletions are localized over some spots where the horizontal crustal field is at a local maximum. The contours of the majority of these regions with enhanced depletions occurrence are in good agreement with the extension of the strong crustal magnetic field sources. Hence, this

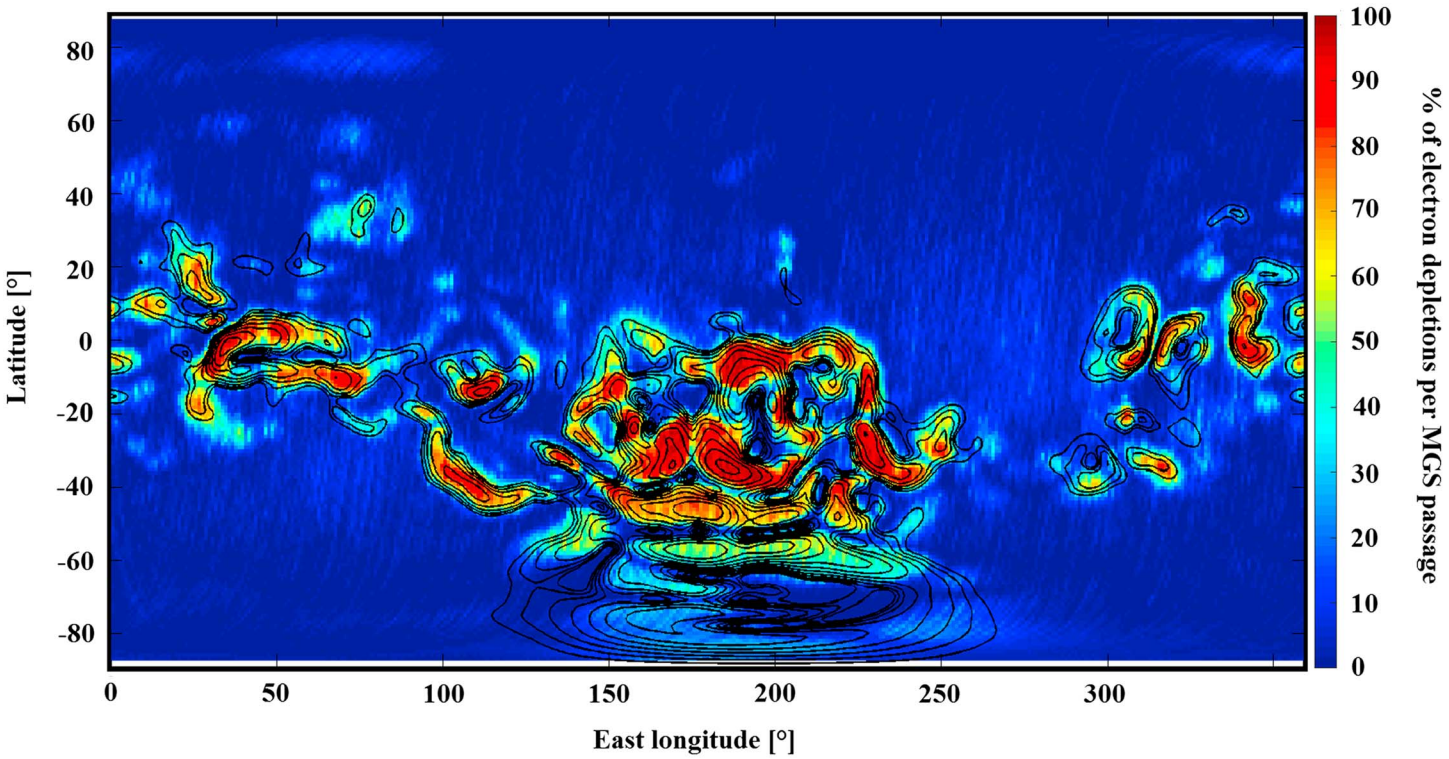

Figure 4. In color, the percentages of electron depletions detected with criterion (3) from MGS data per MGS passage on the nightside on a geographic map of the Martian surface with constant bin size of 1° by 1°. In black, the horizontal magnetic field contour lines calculated from the model of Morschhauser at an altitude of 400 km. The contour lines have been plotted for horizontal crustal fields of 10, 13, 16, 20, 25, 32, 40, 50, 63, 79, and 100 nT.

map confirms the strong link existing between electron depletions and horizontal crustal magnetic field at 400 km. However, we can see that some depletions are located over weak horizontal crustal magnetic field areas such as [340°E, 20°N] or are slightly shifted from the nearest crustal magnetic field source location such as [200°E, 20°N]. Such depletions away from crustal magnetic sources may indicate the presence of loops of closed magnetic field connecting together crustal magnetic field sources in widely separated locations [*Brain et al*., 2007]. We can also notice that the large area with high horizontal crustal magnetic field at high negative latitudes does not fit well with high electron depletion density area. This effect may be due to the inclination of Mars on its orbit, which is about 25°. This implies seasons during which part of the polar regions are always in sunlight, whereas they are considered as being in the nightside due to the use of the MSO coordinates. Thus, no depletions are detected, but these periods are taken into account as MGS passages in the nightside. We will be able to compare this effect with MEX results in the next section (MAVEN does not cover this region).

The presence of permanent (100% of electron depletions detected per MGS passage in the nightside) and intermittent electron depletions can also be observed, as first reported by *Lillis and Brain* [2013]. The permanent depletions seem to be coincident with the strongest horizontal crustal magnetic fields, whereas the intermittent ones are located over weaker crustal magnetic sources or on the border of the strongest ones.

4.2. Mars Express

Figure 5 shows the density map of the electron depletions evaluated with criterion (2). We chose to divide the surface of Mars into spatial bins of 2° by 2°, as there are less data points than for MGS (Table 2). The color code corresponds to the percentage of electron depletions per MEX passage. For each bin we calculated the ratio between the number of time steps when an electron depletion is detected and the total number of time steps when MEX is in the nightside with an altitude below 900 km. There are on average 500 MEX observation time steps per bin. We have also superimposed logarithmically spaced (between 10 and 100 nT) contour lines

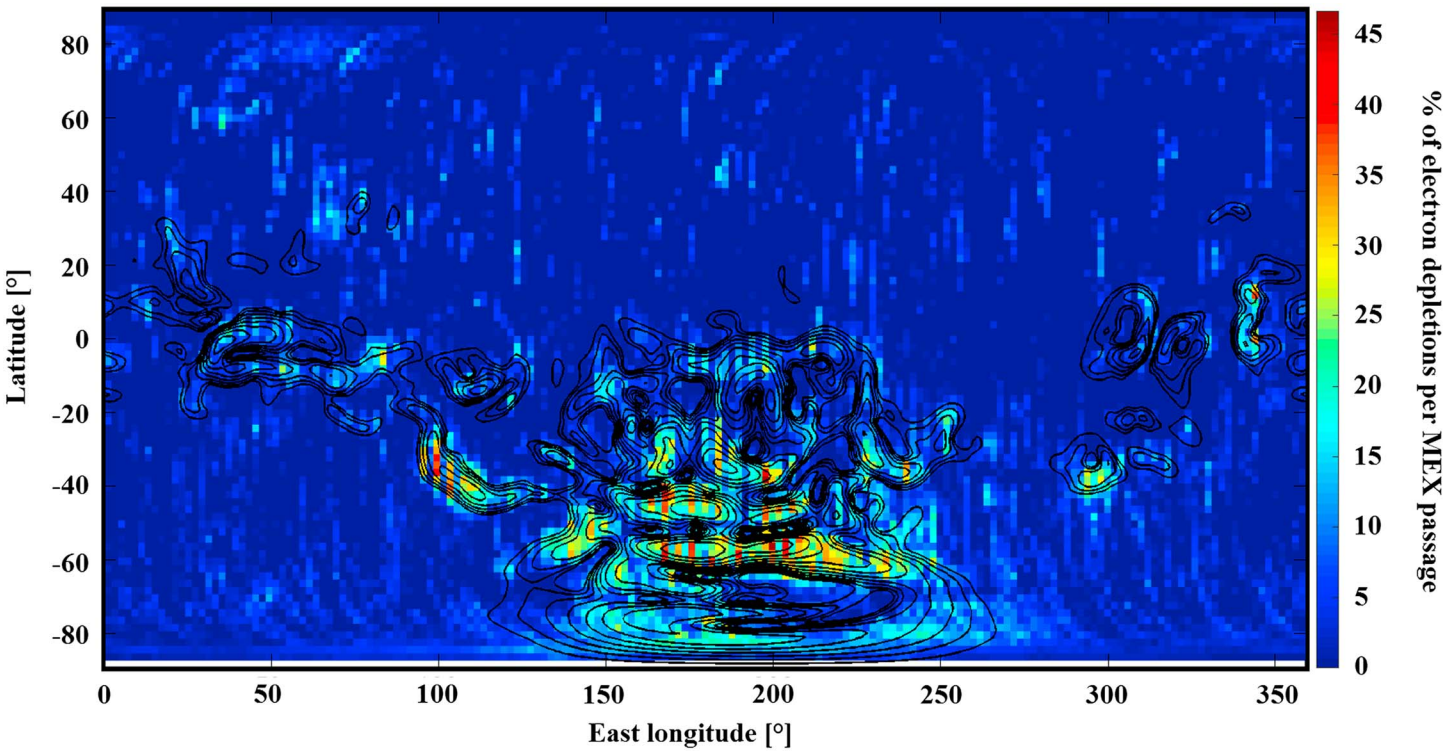

Figure 5. In color, the percentages of electron depletions detected with criterion (2) from MEX data per MEX passage on the nightside on a geographic map of the Martian surface with constant bin size of 2° by 2°. In black, the horizontal magnetic field contour lines calculated from the model of Morschhauser at an altitude of 400 km. The contour lines have been plotted for horizontal crustal fields of 10, 13, 16, 20, 25, 32, 40, 50, 63, 79, and 100 nT.

of the horizontal crustal magnetic field calculated at 400 km altitude from the Morschhauser model so that the maps of MEX and MGS can be compared.

As for MGS, we can see that the electron depletions are globally localized over regions of strong horizontal crustal magnetic field. This supports the idea that, above ~300 km, the main mechanism responsible for electron depletions is still the exclusion by closed crustal magnetic loops. Some electron depletions can still be found over areas without strong crustal magnetic field such as [40°E, 60°N]. However, we can see on this map that the areas with strong crustal fields located at high southern latitudes are now in a better agreement with the distribution of electron depletions. This difference with MGS may be due to the different ways MGS and MEX covered the Martian surface. MGS covered each latitude on the nightside on each orbit, whereas MEX periapsis only covers the southern pole during specific periods. Thus, depending on the seasons when these periods occurred, the percentages obtained in the southern pole region are modified.

The percentages found in Figure 5 are much lower than those found in Figure 4 with MGS and do not enable us to analyze the presence of permanent and intermittent depletions. However, these percentages seem quite similar to those found by *Hall et al*. [2016]. Using the depletions automatically detected thanks to their criterion, *Hall et al*. [2016] produced an occurrence map of the electron depletions observed with MEX during the same time period with a resolution of 15° by 15°, in order to emphasize large-scale occurrences. Their map highlights several areas where electron depletions are concentrated, which are consistent with the ones observed in Figure 5 like the regions centered on [300°E, −40°S] or [200°E, −60°S]. The two maps are comparable except for the regions centered on [200°E, −10°S], where *Hall et al*. [2016] found their maximum occurrence of depletions. We here found for this region a percentage of ~15 % with no real extension toward the Northern Hemisphere but rather toward the Southern Hemisphere where the maximum percentages are located, coincident with the strongest horizontal crustal magnetic fields. Figures 5 and 4 also reveal the presence of electron depletions in the region centered on [70°E, 80°N], where a small crustal magnetic source exists, but which is not observed by *Hall et al*. [2016], maybe due to the resolution chosen by the authors.

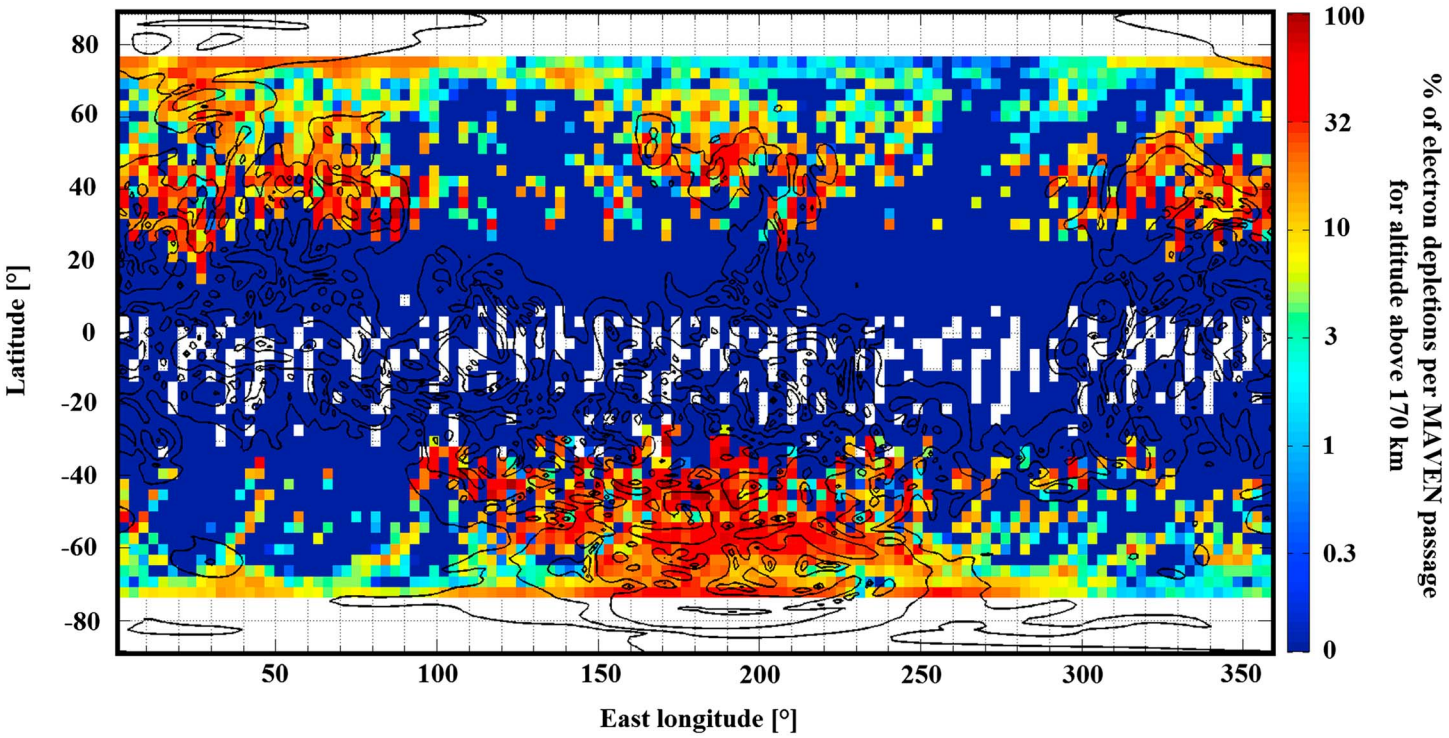

Figure 6. In color, the percentages of electron depletions detected above 170 km with criterion (1) from MAVEN data per MAVEN passage on the nightside on a geographic map of the Martian surface with constant bin size of 3° by 3°. In black, the horizontal magnetic field contour lines calculated from the model of Morschhauser at an altitude of 170 km. The contour lines have been plotted for horizontal crustal fields of 10, 32, 100, 316, and 1000 nT.

As was also mentioned by *Hall et al*. [2016], Figure 4 shows that the regions with strong concentration of electron depletions are surrounded by regions having moderate occurrence rate. Finally, the noise observed in Figure 5 has also been detected by *Hall et al*. [2016], who found a background level around 10% present all over their map. We here tend to limit this noise by selecting events on the nightside and at altitudes below 900 km.

4.3. MAVEN

While MGS was at an altitude of ~400 km and MEX has its lower periapsis at 245 km, MAVEN can reach altitudes down to 125 km during its deep-dip campaigns, which enables a more comprehensive view of the electron depletion phenomenon. Figures 6 and 7 show the density maps of electron depletions detected with MAVEN. In the same way as for the map of MGS and MEX, we calculated the number of time steps when electron depletions are detected in spatial bins of 3° longitude by 3° latitude and divided it by the number of time steps when MAVEN is in the nightside in each bin. Since *Steckiewicz et al*. [2015] showed that the electron depletion distribution was different for altitudes below and above 160–170 km in the Northern Hemisphere, we here provide two maps, the first for altitudes above 170 km and below 900 km (Figure 6) and the second for altitudes below 160 km (Figure 7). This choice enables us to emphasize the differences between the distributions of electron depletions at low and high altitudes. The density maps are superimposed with a map of the horizontal crustal field calculated at 170 km with the Morschhauser model. The contour lines are logarithmically spaced between 10 and 1000 nT. Larger bins of 3° by 3° have been chosen for MAVEN as there are less data than for MEX and MGS (Table 2). On average, there are 280 time steps per bin in Figure 6 and 90 in Figure 7.

In Figure 6, for events at altitudes greater than 170 km, we found the same behavior as for MEX and MGS: the depletions are aggregated on areas of strong horizontal crustal magnetic fields. The variability of the percentage of electron depletions per MAVEN passage seems to support the idea of permanent and intermittent electron depletions. Hence, percentages close to 100% are preferentially seen near the local maxima of

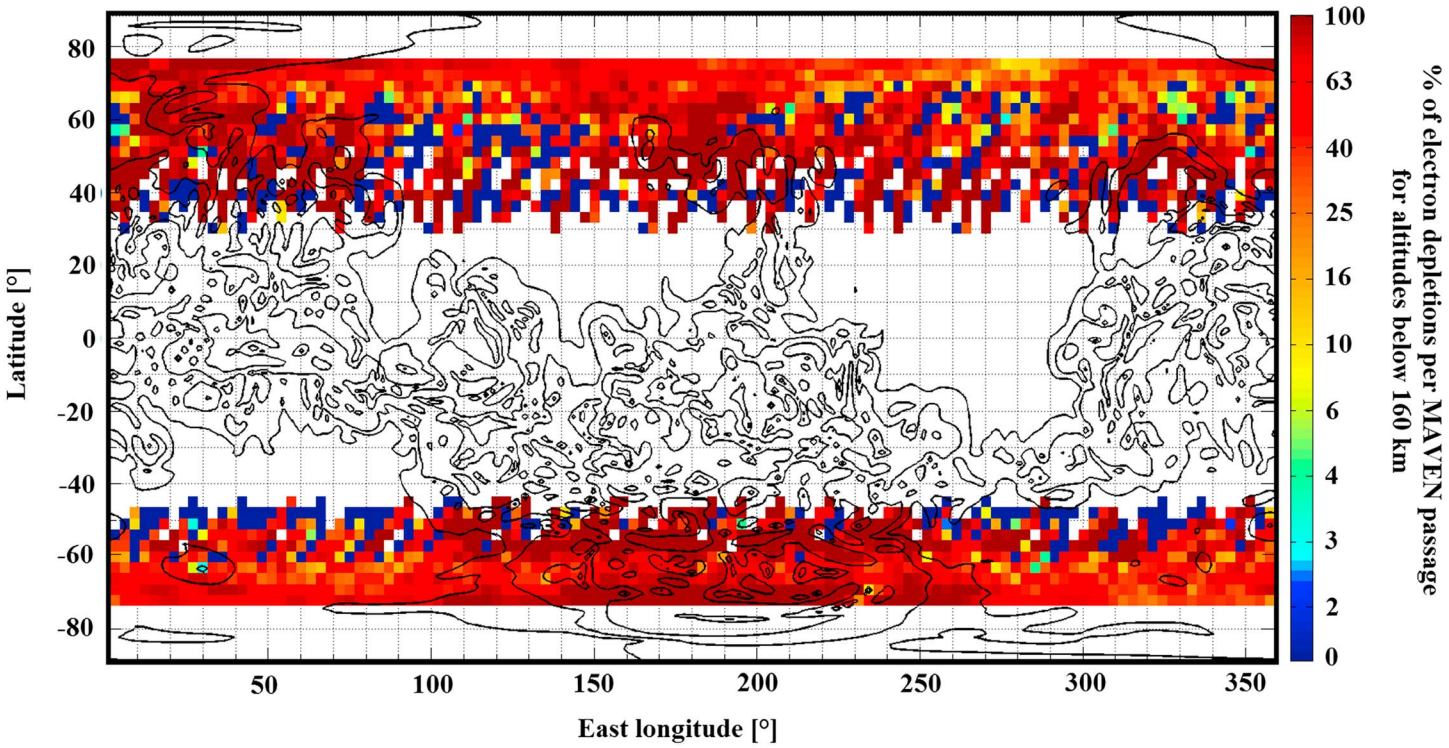

Figure 7. In color, the percentages of electron depletions detected below 160 km with criterion (1) from MAVEN data per MAVEN passage on the nightside on a geographic map of the Martian surface with constant bin size of 3° by 3°. In black, the horizontal magnetic field contour lines calculated from the model of Morschhauser at an altitude of 170 km. The contour lines have been plotted for horizontal crustal fields of 10, 32, 100, 316, and 1000 nT.

horizontal crustal fields, whereas lower percentages are observed far from crustal magnetic field sources, which means that electron depletions are not always present when MAVEN observes these regions. However, as the MAVEN coverage is still not complete, we cannot affirm that permanent depletions are surrounded by intermittent ones as it was observed on MGS distribution but we can see a trend emerge. In Figure 7, for events at altitudes lower than 160 km, we can see that the higher percentage of electron depletions are still localized above strong crustal magnetic field sources, but we can notice that the global distribution is far more homogeneous than for the distribution above 170 km, regardless of the horizontal magnetic field. Thus, closed crustal magnetic loops are still an important process responsible for electron depletions. However, there is also another important process which is involved and which does not depend a priori on crustal magnetic field, like electron absorption by atmospheric CO_2. The study of the Southern Hemisphere of Mars confirms the fact that the distribution of electron depletions is highly dependent on altitude.

5. Altitude Dependence of Electron Depletion Distribution

In *Steckiewicz et al*. [2015] we showed that the altitude distribution of electron depletions detected by MAVEN observations in the Northern Hemisphere was different above and below a transition region near 160–170 km altitude. There were far more chances to detect an electron depletion during a passage of MAVEN below this region than above. Here we complement this study with data from MAVEN above the Southern Hemisphere midlatitudes and data from MEX above both hemispheres. The time periods studied are, respectively, the same as for the previous section.

5.1. Description of the Method

Since the MAVEN data currently only cover latitudes northward of ~20° and southward of ~−20°, we only include MEX observations of the electron depletions detected in the same range of latitudes. We have also studied the Northern and the Southern Hemispheres separately. For both spacecraft we took an altitude

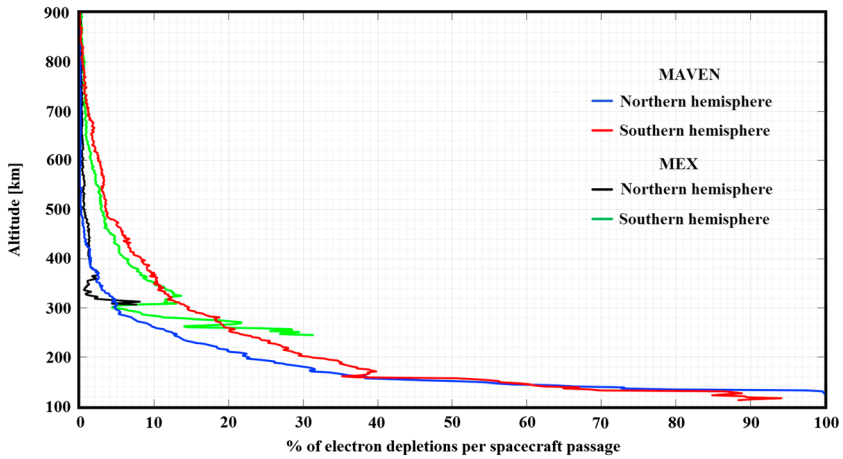

Figure 8. Percentages of electron depletions detected by criterion (1) among MAVEN passages (in blue and red) and by criterion (2) among MEX passages (in black and green) calculated in bins of 2 km altitude. The red and green lines correspond to the depletions observed in the Southern Hemisphere, and the red and black lines correspond to the depletions detected in the Northern Hemisphere.

resolution of 2 km, which represents ~10,000 MEX passages per bin and ~2600 MAVEN passages per bin on average. For each bin we calculated the number of time steps when electron depletions are detected and the number of time steps when the spacecraft is in the nightside. The ratio gives the percentage of electron depletions among the spacecraft passages in each altitude bin. The MGS observations previously discussed are not applicable to this analysis, since the spacecraft had a circular orbit with an almost constant altitude.

5.2. Results

Figure 8 shows the percentage of electron depletions detected along the MAVEN and MEX passages as a function of altitude. The red and green profiles correspond to the observations made by MAVEN and MEX, respectively, above the Southern Hemisphere, while the blue and black profiles correspond to the observations made by MAVEN and MEX, respectively, above the Northern Hemisphere. We can notice that MEX data are only available down to 307 km in the Northern Hemisphere, whereas they are available down to 245 km in the Southern Hemisphere. This difference is only due to MEX orbital geometry.

We can see that the MEX and MAVEN results match well between 900 and 300 km. In this range of altitude, both data sets show that there is far more chance to detect an electron depletion in the Southern Hemisphere than in the Northern Hemisphere. This phenomenon seems to be due to the presence in the Southern Hemisphere of stronger crustal magnetic sources than in the Northern Hemisphere. Hence, the closed crustal magnetic loops can extend higher in the Southern Hemisphere than in the Northern Hemisphere. Between 300 and 245 km, even though data are no more recorded by MEX in the Northern Hemisphere, there are still some in the Southern Hemisphere. Although strong variations can be observed on MEX data, we can see that the profile follows the trend set by MAVEN data. These variations may be due to the range of altitudes, which is beneath the nominal periapsis and hence sparsely covered by the spacecraft.

For altitudes greater than 500 km, *Hall et al*. [2016] found that the normalized occurrence of electron depletions was less than 5% across the majority of latitudes and altitudes, except for the strongest crustal magnetic field regions around which the majority of the events are distributed and where enhanced occurrence are then detected up to 1000 km. This is consistent with the results obtained in Figure 8 even if the percentages are lower than those found by *Hall et al*. [2016]: 1% in the Northern Hemisphere and 3% in the Southern Hemisphere at 500 km. Below 500 km, the occurrence of electron depletions increases rapidly in both studies. The main difference is that *Hall et al*. [2016] found that the distribution of electron depletions becomes more homogeneous below 500 km, even if the highest occurrences are still located above the strongest crustal magnetic field areas. In Figure 8 we clearly see that there are more electron depletions detected by MEX in the Southern Hemisphere than in the Northern Hemisphere, at least until 300 km. The difference between the two hemispheres even increases between 500 km and 300 km.

Where MEX ceases to record data, MAVEN continues to observe electron depletions at lower altitudes. We can see that the difference in percentage between the Southern and the Northern Hemispheres persists until a transition region near 160–170 km altitude, where the two curves join and stay close until 125 km. Hence, at low altitudes the electron depletion distribution does not depend on the hemisphere nor on the presence of crustal magnetic sources. This result reinforces the conclusions of *Steckiewicz et al*. [2015] about the presence of two processes responsible for electron depletions, each of them being predominant in a specific altitude regime. Depletion events above 160–170 km altitude are predominantly produced by the exclusion of suprathermal electrons by closed crustal magnetic fields, whereas events below 160–170 km are predominantly produced by absorption by atmospheric CO_2. The study of the Southern Hemisphere with MAVEN data also shows that the transition between the altitude regimes seems to be the same in both hemispheres, regardless the intensity of the crustal magnetic sources.

6. Conclusions

In this paper we have analyzed observations of electron depletions from three different Martian missions (MGS, MEX, and MAVEN) in order to better characterize their altitude and geographical distributions and understand their formation processes. We thus provide here the first multispacecraft analysis of electron depletions covering 17 years of Martian exploration, offering a comprehensive view of the phenomenon.

While previous studies used different approaches to identify electron depletions in MGS and MEX data, we here used the same method to automatically detect these events in the three Martian orbiter data sets. In addition, we did not impose any geometric restrictions in our conditional research—contrary to previous studies like the one of *Hall et al*. [2016], which was restricted to the illuminated induced magnetosphere.

Our results show that electron depletions are spread on the nightside of the Martian environment at altitudes between 110 and 900 km. For comparable altitude ranges (i.e., above about 250 km), the aerographic distributions of electron depletions for each mission produced result in agreement with each other and with previous studies: electron depletions are strongly linked with the horizontal crustal magnetic fields. The study of *Steckiewicz et al*. [2015] has been extended to the Southern Hemisphere of Mars at low altitudes and has confirmed this link with the crustal magnetic sources until a transition region near 160–170 km altitude regardless the hemisphere (and thus regardless of the intensity of the crustal magnetic sources). It was obviously not possible to identify this transition region with MGS and MEX due to their altitude limitations (~400 km for MGS and greater than 245 km for MEX). The comparison of the altitudinal distribution of the electron depletions detected in both hemispheres by MEX and MAVEN showed that above this transition region far more depletions are observed above the Southern Hemisphere, where the strongest crustal magnetic field sources are located. The crustal fields thus act as a barrier preventing the replenishing of the electron-depleted area (depleted due to the absence of solar EUV photoionization) by external incoming electrons. However, below the transition region at 160–170 km, the MAVEN data have revealed that the distribution is globally homogeneous in latitude-longitude and between both hemispheres. Thus, at low altitudes crustal magnetic fields are no longer predominant in the creation of electron depletions, further suggesting that the denser atmospheric CO_2 population is responsible for creating the depletions at those altitudes by absorption processes [*Steckiewicz et al*., 2015].

One original application of our study is using nightside suprathermal electron depletions as an indirect method of detecting crustal fields allowing the determination of the topology of the magnetic field using electron spectrometers [*Mitchell et al*., 2007; *Brain et al*., 2007]. Closed magnetic field lines are indeed associated with the Martian crustal magnetic fields and can be identified in the nightside by the presence of electron depletions notably at altitudes above approximately 170 km.

As studied by *Hall et al*. [2016], electron depletions can be observed to some extent in the terminator region. The processes creating electron depletions in regions illuminated or in shadow could be different. The electron depletion distributions obtained in the dawn and the dusk sector are also expected not to be the same since the photoelectrons—liberated on the dayside of Mars mainly from ionization of atmospheric CO_2 and O by solar photons—are travelling from the dayside to the nightside following the rotation of the planet. A delay is expected on the duskside for the electrons to be depleted. A study of the distribution of electron depletion with respect to local time and solar zenith angle will be made when the complete local time coverage will be achieved by MAVEN and reported in a future paper.

Acknowledgments
This work has been supported by the French Space Agency CNES for the part based on observations obtained with the SWEA instrument on MAVEN. The MAVEN project is supported by NASA through the Mars Exploration Program. The authors acknowledge the support of the MAVEN project and particularly of the instrument and science teams. Data analysis was performed with the AMDA science analysis system (http://amda.cdpp.eu) provided by the Centre de Données de la Physique des Plasmas CDPP supported by CNRS; CNES; Observatoire de Paris; and Université Paul Sabatier, Toulouse, France. The MGS, MEX, and MAVEN data used in this paper are publicly available through the Planetary Data System (http://ppi.pds.nasa.gov/). The authors sincerely thank the two anonymous reviewers for their constructive comments.

References

Acuña, M. H., et al. (2001), Magnetic field of Mars: Summary of results from the aerobraking and mapping orbits, *J. Geophys. Res.*, *106*, 23,403–23,417, doi:10.1029/2000JE001404.

Albee, A. L., R. E. Arvidson, F. Palluconi, and T. Thorpe (2001), Overview of the Mars Global Surveyor mission, *J. Geophys. Res.*, *106*, 23,291–23,316, doi:10.1029/2000JE001306.

Andersson, L., R. E. Ergun, G. T. Delory, A. I. Eriksson, J. Westfall, H. Reed, J. McCauly, D. Summers, and D. Meyers (2015), The Langmuir Probe and Waves instrument for MAVEN, *Space Sci. Rev.*, *195*, 173–198, doi:10.1007/s11214-015-0194-3.

Barabash, S., et al. (2004), ASPERA-3: Analyser of Space Plasmas and Energetic Ions for Mars Express, in *Mars Express: the Scientific Payload (ESA SP-1240)*, edited by A. Wilson and A. Chicarro, 121 pp., ESA, Noordwijk, Netherlands.

Bertucci, C., et al. (2003), Magnetic field draping enhancement at the Martian magnetic pileup boundary from Mars Global Surveyor observations, *Geophys. Res. Lett.*, *30*(2), 1099, doi:10.1029/2002GL015713.

Bougher, S., et al. (2015), Early MAVEN deep dip campaigns: First results and implications, *Sciences*, *350*(6261), doi:10.1126/science.aad0459.

Brain, D. A., F. Bagenal, M. H. Acuña, and J. E. P. Connerney (2003), Martian magnetic morphology: Contributions from the solar wind and crust, *J. Geophys. Res.*, *108*(A12), 1424, doi:10.1029/2002JA009482.

Brain, D. A., R. J. Lillis, D. L. Mitchell, J. S. Halekas, and R. P. Lin (2007), Electron pitch angle distributions as indicators of magnetic field topology near Mars, *J. Geophys. Res.*, *112*, A09201, doi:10.1029/2007JA012435.

Chicarro, A., P. Martin, and R. Trautner (2004), The Mars Express mission: An overview, Planetary Missions Division, Research & Scientific Support Department, ESA/ESTEC, PO box 299, 2200 AG Noordwijk, Netherlands.

Connerney, J. E. P., J. Espley, P. Lawton, S. Murphy, J. Odom, R. Oliverson, and D. Sheppard (2015), The MAVEN magnetic field investigation, *Space Sci. Rev.*, doi:10.1007/s11214-015-0169-4.

Duru, F., D. A. Gurnett, D. D. Morgan, J. D. Winningham, R. A. Frahm, and A. F. Nagy (2011), Nightside ionosphere of Mars studied with local electron densities: A general overview and electron density depressions, *J. Geophys. Res.*, *116*, A10316, doi:10.1029/2011JA016835.

Fillingim, M. O., L. M. PetiColas, R. J. Lillis, D. A. Brain, J. S. Halekas, D. Lummerzheim, and S. W. Bougher (2010), Localized ionization patches in the nighttime ionosphere of Mars and their electrodynamic consequences, *Icarus*, *206*, 112–119, doi:10.1016/j.icarus.2009.03.005.

Frahm, R. A., et al. (2006), Locations of atmospheric photoelectron energy peaks within the Mars environment, *Space Sci. Rev.*, *126*, 389–402, doi:10.1007/s11214-006-9119-5.

Fränz, M., E. Dubinin, E. Roussos, J. Woch, J. D. Winningham, R. Frahm, A. J. Coates, A. Fedorov, S. Barabash, and R. Lundin (2006), Plasma moments in the environment of Mars: Mars Express ASPERA-3 observations, *Space Sci. Rev.*, *126*, 165–207, doi:10.1007/s11214-006-9115-9.

Fränz, M., E. Dubinin, E. Nielsen, J. Woch, S. Barabash, R. Lundin, and A. Fedorov (2010), Transterminator ion flow in the Martian ionosphere, *Planet. Space Sci.*, *58*, 1442–1454, doi:10.1016/j.pss.2010.06.009.

Hall, B. E. S., M. Lester, J. D. Nichols, B. Sánchez-Cano, D. J. Andrews, H. J. Opgenoorth, and M. Fränz (2016), A survey of suprathermal electron flux depressions, or 'electron holes', within the illuminated Martian induced magnetosphere, *J. Geophys. Res. Space Physics*, *121*, 4835–4857, doi:10.1002/2015JA021866.

Jakosky, B. M., J. M. Grebowsky, J. G. Luhmann, and D. A. Brain (2015), Initial results from the MAVEN mission to Mars, *Geophys. Res. Lett.*, *42*, 8791–8802, doi:10.1002/2015GL065271.

Krasnopolsky, V. A. (2002), Mars' upper atmosphere and ionosphere at low, medium and high solar activities: Implications for evolution of water, *J. Geophys. Res.*, *107*(E12), 5128, doi:10.1029/2001JE001809.

Lillis, R. J., and D. A. Brain (2013), Nightside electron precipitation at Mars: Geographic variability and dependence on solar wind conditions, *J. Geophys. Res. Space Physics*, *118*, 3546–3556, doi:10.1002/jgra.50171.

Lillis, R. J., H. V. Frey, and M. Manga (2008), Rapid decrease in Martian crustal magnetization in the Noachian era: Implications for the dynamo and climate of early Mars, *Geophys. Res. Lett.*, *35*, L14203, doi:10.1029/2008GL034338.

Lillis, R. J., M. O. Fillingim, and D. A. Brain (2011), Three-dimensional structure of the Martian nightside ionosphere: Predicted rates of impact ionization from Mars Global Surveyor magnetometer and Electron Reflectometer measurements of precipitating electrons, *J. Geophys. Res.*, *116*, A12317, doi:10.1029/2011JA016982.

Lillis, R. J., S. Robbins, M. Manga, J. Halekas, and H. V. Frey (2013), Time history of the Martian dynamo from crater magnetic field analysis, *J. Geophys. Res. Planets*, *118*, 1488–1511, doi:10.1002/jgre.20105.

Ma, Y., X. Fang, C. T. Russell, A. F. Nagy, G. Toth, J. G. Luhmann, D. A. Brain, and C. Dong (2014), Effects of crustal field rotation on the solar wind plasma interaction with Mars, *Geophys. Res. Lett.*, *41*, 6563–6569, doi:10.1002/2014GL060785.

McFadden, J. P., et al. (2015), MAVEN Suprathermal and Thermal Ion Composition (STATIC) instrument, *Space Sci. Rev.*, *195*(1–4), 199–256, doi:10.1007/s11214-015-0175-6.

Mitchell, D. L., R. P. Lin, C. Mazelle, H. Rème, P. A. Cloutier, J. E. P. Connerney, M. H. Acuña, and N. F. Ness (2001), Probing Mars' crustal magnetic field and ionosphere with the MGS Electron Reflectometer, *J. Geophys. Res.*, *106*, 23,419–23,427, doi:10.1029/2000JE001435.

Mitchell, D. L., R. J. Lillis, R. P. Lin, J. E. P. Connerney, and M. H. Acuña (2007), A global map of Mars' crustal magnetic field based on elecron reflectometry, *J. Geophys. Res.*, *112*, E01002, doi:10.1029/2005JE002564.

Mitchell, D. L., et al. (2016), The MAVEN Solar Wind Electron Analyzer, *Space Sci. Rev.*, *200*, 495–528, doi:10.1007/s11214-015-0232-1.

Morschhauser, A., V. Lesur, and M. Grott (2014), A spherical harmonic model of the lithospheric magnetic field of Mars, *J. Geophys. Res. Planets*, *119*, 1162–1188, doi:10.1002/2013JE004555.

Nagy, A. F., et al. (2003), The plasma environment of Mars, *Space Sci. Rev.*, *111*, 33–114, doi:10.1023/B:SPAC.0000032718.47512.92.

Němec, F., D. D. Morgan, D. A. Gurnett, and F. Duru (2010), Nightside ionosphere of Mars: Radar soundings by the Mars Express spacecraft, *J. Geophys. Res.*, *115*, E12009, doi:10.1029/2010JE003663.

Soobiah, Y., et al. (2006), Observations of magnetic anomaly signatures in Mars Express ASPERA-3 ELS data, *Icarus*, *182*, 396–405, doi:10.1016/j.icarus.2005.10.034.

Steckiewicz, M., et al. (2015), Altitude dependence of nightside Martian suprathermal electron depletions as revealed by MAVEN observations, *Geophys. Res. Lett.*, *42*, 8877–8884, doi:10.1002/2015GL065257.

Ulusen, D., and I. R. Linscott (2008), Low-energy electron current in the Martian tail due to reconnection of draped interplanetary magnetic field and crustal magnetic fields, *J. Geophys. Res.*, *113*, E06001, doi:10.1029/2007JE002916.

Withers, P., M. O. Fillingim, R. J. Lillis, B. Häusler, D. P. Hinson, G. L. Tyler, M. Pätzold, K. Peter, S. Tellmann, and O. Witasse (2012), Observations of the nightside ionosphere of Mars by the Mars Express Radio Science Experiment (MaRS), *J. Geophys. Res.*, *117*, A12307, doi:10.1029/2012JA018185.

Zhang, M. H. G., J. G. Luhmann, and A. J. Kliore (1990), An observational study of the nightside ionospheres of Mars and Venus with radio occultation methods, *J. Geophys. Res.*, *95*, 17,095–17,17102, doi:10.1029/JA095iA10p17095.